Indonesian Physical Review
Volume 6 Issue 1, January 2023
P-ISSN: 2615-1278, E-ISSN: 2614-7904

First-Principles Study of Magnetic Anisotropy Energy in Two-Dimensional Ferromagnetic CrI_3

Puke Lajaladita Litle Mecci[1], Annisa Monica[1], Iin Riananda Br Sinurat[2], Agustina Widiyani[1], Abdul Rajak[1], Indra Pardede[1*]
[1] *Department of Physics, Faculty of Science, Sumatera Institute of Technology, Indonesia.*
[2]*Master Program of Physics, Faculty of Science, Sumatera Institute of Technology, Indonesia.*

Corresponding Authors E-mail: indra.pardede@fi.itera.ac.id

Article Info

Article info:
Received: 30-08-2022
Revised: 16-12-2022
Accepted: 19-12-2022

Keywords :
Ferromagnetic material; 2D monolayer CrI_3; Magnetic anisotropy energy (MAE); First-principles calculation

How To Cite :
P. L. L. Mecci, A, Monica, I. Riananda, A. Widiyani, A. Rajak, I. Pardede, "First-Principles Study of Magnetic Anisotropy Energy in Two-Dimensional Ferromagnetic CrI_3", Indonesian Physical Review, vol. 6, no. 1, p 60-84, 2023.

DOI :
https://doi.org/10.29303/ipr.v6i1.191.

ABSTRACT

*First-principles calculations are increasingly crucial in searching for new materials with customized properties or new functionality. First-principles calculations are superior in speed and cost, and comparable to experiments in terms of accuracy. Two-dimensional (2D) ferromagnetism materials were successfully fabricated experimentally in atomic thin films of CrI_3. 2D intrinsic ferromagnetism with perpendicular magnetic anisotropy energy (PMAE) is an encouraging applicant compatible with high-density magnetic storage applications. In this study, spin density functional calculations are investigated on the magnetic anisotropy energy (MAE) in 2D monolayer ferromagnetic CrI_3 using a first-principles electronic structure calculation. We include the MAE part calculation from the magnetocrystalline anisotropy energy (MCAE) that comes from the spin-orbit coupling (SOC). In the present calculation, the MCAE part, in addition to a usual scheme of total energy (TE), was evaluated using a grand-canonical force theorem (GCFT) scheme. The MCAE of 2D monolayer ferromagnetic CrI_3 is 1.7 meV/unit cell and verified it has an easy-axis perpendicular to the crystal plane, which is a good agreement with experimental measurement. In the latter scheme, employing GCFT, we evaluated atom-resolved, **k**-resolved, and atomic **k**-resolved analyses for MCAE can be performed. From the GCFT result, the Cr atom indicates that it is the primary origin of PMAE in the atom-resolved MCAE. The negative MCAE contribution is in $\bar{\Gamma}$ points, and the positive MCAE is mainly placed at the line $\bar{K}-3/4\bar{K}\bar{\Gamma}$ in the 2D first Brillouin zone. Our systematic calculation in this work may also help design an effective structure of monolayer CrI_3 in new 2D material magnetic sensor and spintronic device designs.*

Introduction

Over the centuries, science and technology as a whole have experienced rapid developments, and this development is also in line with how the field of materials science has developed. For thousands of years, science was pristine experimental, with metallurgical observations

during the "age" (steel, stone, iron, and bronze). Then the theoretical model paradigm emerged and was generally characterized by formulating various "laws" in mathematical equations, such as the laws of thermodynamics, Newton's laws, and Maxwell's equations. But for numerous scientific difficulties, theoretical models become too involved or complex for analytical methods, and one has to start simulating. The third paradigm of computational science looked good on greatly prevalent with computer power some decades ago. Very good instances of this in materials science are molecular dynamics and density functional theory (DFT) simulation. Furthermore, a fourth scientific paradigm has emerged over the last some years due to the quantity of data produced by experiments and simulations. This is science driven by (big) data. It is appropriate and progressively prevalent in the field of materials science as well and, in fact, has caused the becoming known of a recent lot of materials informatics [1][2].

For the forecast, the properties of materials from the arrangement of their atoms are the main target of materials science. The first-principles calculation can make the most reliable material properties prediction [3]. Magnetic phenomena are important in science and technology. Magnetic materials are at the core of many modern technological applications. For example, magnetic materials are used for sensors, data storage, and biosensor [2]. For example, magnetic random-access memory (MRAM) is a type of random-access memory. In fundamental, MRAM uses the effect of magnetoresistance for the reading process [4].

Several research areas have rapidly advanced over the past decade, including electronics, batteries, photonics, and catalysis for two-dimensional (2D) materials. These developments have led to the constant discovery of new 2D materials, supported by the attractive and tuneful properties of atomic thin crystals. 2D materials have also opened up opportunities for scheming materials with customized and good properties [5]. The finding of 2D magnetism wide opens the gates for discovering spintronic and sensor nanodevices [6][7]. As a platform for studying new physical phenomena, 2D magnetic materials have interesting research concerns whole the world. In the manner of the Mermin-Wagner theorem, thermal inconstancy can efficiently remove 2D magnetism in the isotropic Heisenberg design at a limited temperature. On the other hand, magnetic anisotropy can discard this constraint, thus giving one to get 2D intrinsic ferromagnetism. As a consequence, magnetic anisotropy is a condition component of 2D intrinsic ferromagnetism [8]. After continuous research, several 2D magnets were successfully fabricated experimentally. In 2017, 2D intrinsic ferromagnetism was discovered experimentally, i.e., including the monolayer CrI_3 [9] and the bilayer $Cr_2Ge_2Te_6$ [10].

Since 2D materials can be considered atomic thin films, for applications in high-density magnetic storage of, 2D intrinsic ferromagnetism with perpendicular magnetic anisotropy (PMA) is an encouraging worthy candidate [8]. In this case, magnetic anisotropy is a magnetic energy that is conditional on the direction of magnetization [11]. Investigation of newly discovered 2D magnetics escorted by elevated transition temperatures and of considerable size PMA is still significant defiance and essential for fundamental research and future applications. The high MAE also indicates excellent potential for applications in low-energy spintronics [7]. Consequently, much effort has been invested in investigating 2D intrinsic ferromagnetic PMA [8].

First-principles calculations are increasingly crucial in searching for recently developed materials with customized properties or else new functionality. First-principles calculations

are superior in speed and cost and comparable to experiments in terms of accuracy [5]. 2D monolayer ferromagnetic CrI_3 is one of the magnetic materials with easy-axis anisotropy perpendicular to the atomic plane. It was forecast out of the first-principles computation that 2D monolayer ferromagnetic CrI_3 has perpendicular magnetic anisotropy properties [12][13][14]. A similar conclusion was as well informed by the experimental measurements [9]. In their performance, the specifics of magnetic properties, such as total magnetic anisotropy, magnetization, and spin polarization were examined, as a potential application for spintronics. However, the detail of the origin of magnetocrystalline anisotropy energy (MCAE) and the contribution from the Cr atom and I atom was not discussed in their investigation. In the investigation of MCAE, atom-resolved or **k**-resolved MCAE has been helpful to analyse magnetic anisotropy. That analyzing the **k**-resolved contribution can facilitate us to explain the local **k**-space contribution to positive or negative MCAE by relating it to the electronic structure. This may be basically because the physical amount of MCAE is susceptible to the occupation of electrons close to the Fermi level. Furthermore, **k**-resolved MCAE is as well important to explain the effect of electric fields on the MCAE [15][16].

In this work, spin density functional calculations are performed on 2D monolayer ferromagnetic CrI_3 with the same structure as the experimental measurement [9]. This paper is structured as follows and contains a theoretical background of MAE. In particular, the primary origin of MAE arises from the spin-orbit coupling (SOC). In the successive section, explain the computational method that we used in the calculation. The detail of MAE and electronic structure calculation will be described. The results are reported in the next section, followed by discussions. It will start with the result and discussion we presented on MAE contribution from the MCAE arising from the SOC. The source of PMA was entirely in terms of the use of the atom-resolved and **k**-resolved endowment. Next, we continue to discuss the results of the electronic structure monolayer ferromagnetic CrI_3 system. Finally, in the next section, we summarize all results. This research is related to the application of the spin density functional theory (SDFT) scheme to calculate the MAE of 2D monolayer ferromagnetic CrI_3 in Car-Parrinello Vanderbilt Oda (CPVO) code [17][18][19], which makes us fully and scalar relativistic ultrasoft pseudopotentials and plane waves basis [18][20]. The aim is to develop a particularly robust predictive model for calculating MCAE in 2D monolayer ferromagnetic CrI_3. This study also explains the mechanism of the magnitude of MCAE values and aims to stimulate experimental efforts toward 2D magnetic materials for new spintronic devices.

Theoretical Framework

Density Functional Theory

Investigating the electronic structures of atoms, molecules, and solids can be used DFT. DFT is used to simplify solving the Schrodinger equation for many-electrons interaction.
The core quantity of DFT is the electron density [21]:

$$n(\mathbf{r}) = \langle \Phi | \hat{n}(\mathbf{r}) | \Phi \rangle \quad (1)$$

where $|\Phi\rangle$ is a many-body state. In 1964 Hohenberg and Kohn made the DFT full quantum mechanical approach which enables the expression of the electronic Hamiltonian as a function of electron density [22]. Their work is DFT underlying on consists of two main theorems frameworks. The first theorem the total ground-state energy of a many-electron

system is a function of the electron density $n(\mathbf{r})$. In the second Hohenberg-Kohn theorem for the many-electrons system, the function for the minimum total energy is equivalent to the ground state energy at the ground state density.

The usefulness of DFT was reached in 1965 when Kohn and Sham identify a mean-field theory for non-interacting electrons in an effective potential [23]. The basic concept given by Kohn and Sham can be described as the energy function as split into three parts [23],

$$E[n] = \mathrm{T}[n] + \iint \frac{n(\mathbf{r})n(\mathbf{r}')}{|\mathbf{r}-\mathbf{r}'|}\mathrm{d}\mathbf{r}\mathrm{d}\mathbf{r}' + E_{xc}[n], \tag{2}$$

where presented the kinetic, Hartree, and exchange-correlation energy. The kinetic energy of the external field is displaced by an effective external field v_{eff} (named the Kohn-Sham potential). The exchange-correlation energy (E_{xc}) is the contribution of the kinetic energy of the electron correlation effect from every lost quantum effect.
Which is an effective potential given by [23],

$$v_{eff}(\mathbf{r}) = v_{ext}(\mathbf{r}) + 2\int \frac{n(\mathbf{r}')}{|\mathbf{r}-\mathbf{r}'|}\mathrm{d}\mathbf{r}' + v_{xc}(\mathbf{r}) \tag{3}$$

with

$$v_{xc}(\mathbf{r}) = \frac{\delta(E_{xc}+T_{xc})}{\delta n(\mathbf{r})}. \tag{4}$$

This leads to the Kohn-Sham equation which is an effective one-electron equation [23],

$$\left[-\nabla^2 + v_{\mathrm{eff}}(\mathbf{r}) - \varepsilon_i\right]\phi_i(\mathbf{r}) = 0, \tag{5}$$

where ε_i are the energies of the one-electron orbitals ϕ_i. It should be underlined that the Kohn-Sham equations have to be completed self-consistently because v_{eff} the hinge on electron density *n* is determined using the one-electron orbital ϕ_i [23]:

$$n(r) = \sum_{i=1}^{N} |\phi_i(\mathbf{r})|^2 . \tag{6}$$

Now, the total energy is not the sum of the orbital energies $E \neq \sum_i^N \varepsilon_i$ but it may be calculated by the resulting density using [23],

$$E[n] = \sum_{\substack{i=1 \\ \varepsilon_i \le E_F}}^{N} \varepsilon_i - \iint \frac{n(\mathbf{r})n(\mathbf{r}')}{|\mathbf{r}-\mathbf{r}'|}\mathrm{d}\mathbf{r}\mathrm{d}\mathbf{r}' + \tilde{E}_{xc}[n] - \int v_{xc}(\mathbf{r})n(\mathbf{r})\mathrm{d}\mathbf{r}. \tag{7}$$

Magnetocrystalline Anisotropy Energy

Magnetic anisotropy energy (MAE) is the total energy difference between two different magnetization directions. MAE is performed based on the theoretical framework of DFT. The MAE part is performed by contributing the magnetocrystalline anisotropy energy (MCAE) that arises from the spin-orbit coupling (SOC). The MCAE part will be evaluated on the total energy (TE) difference and the grand-canonical force theorem (GCFT).

Total energy difference

The investigated MCAE is included in the spin-orbit interaction on the basis of distinction in total energy among the magnetization parallel (in-plane) and perpendicular (out-of-plane) to the crystal plane. The total energy is conditional on the magnetization heading. The heading of magnetization is expressed as [001], [100] or [010]. Finally, the MCAE is acquired by arresting the total energy distinction among the in-plane and perpendicular magnetization directions as $\mathrm{MCAE} = \mathrm{E}_{\mathrm{tot}}^{[100]} - \mathrm{E}_{\mathrm{tot}}^{[001]}$. The [100] (*x*-axis directions) denote the in-plane magnetization heading, and the [001] (*z*-axis directions) denote the perpendicular magnetization heading to the crystal plane [24].

We use an SDFT to investigate the TE originating from SOC. The TE $E_{\mathrm{SDFT}}[n(\mathbf{r}), \mathbf{m}(\mathbf{r})]$ in the SDFT is described as a function of spin density $\mathbf{m}(\mathbf{r})$ and electron density $n(\mathbf{r})$. $\hat{V}_{\mathrm{eff}}$ is the effective electron potential that is defined through self-consistently as a function of $\mathbf{m}(\rho)$ and *n*. In $\hat{V}_{\mathrm{eff}}$, the SOC potential shall be contained as an expression $V_{\mathrm{SOC}} = \xi \mathrm{L} \cdot \sigma$, with **L** and ξ are an orbital angular moment vector and SOC constant, respectively. Ignoring the SOC ε_i without hinge on the easy axis of the magnetization vector. The total energy of SDFT (E_{SDFT}) is can be presented as [24],

$$E_{\mathrm{SDFT}} = \sum_{i}^{\mathrm{occ.}} \int d\mathbf{r} \Phi_i^*(\mathbf{r}) \left(-\frac{1}{2} \nabla^2 \sigma_0 \right) \Phi_i(\mathbf{r}) + \int d\mathbf{r} n(\mathbf{r}) V_{\mathrm{ext}}(\mathbf{r}) + \frac{1}{2} \iint d\mathbf{r} d\mathbf{r}' \frac{n(\mathbf{r}) n(\mathbf{r}')}{|\mathbf{r} - \mathbf{r}'|} + E_{\mathrm{xc}}[n, \mathbf{m}] + U, \quad (8)$$

where E_{xc} represents exchange-correlation energy as a function of $\mathbf{m}$ and n. V_{ext} describes potential out of the inner core and nuclei states. U indicates the interaction energy among the inner core or nuclei states [24].

Grand-canonical force theorem

Otherwise, MCAE is calculated using a different method, and the approach is built on the magnetic force theorem. It is based on a GCFT [25][26][27]. As an outcome, we may examine the atom-resolved, **k**-resolved, and atomic **k**-resolved endowments of MCAE rationally. In the GCFT method, the MCAE is calculated in view of the SOC acquired by implementing a two-step procedure. First, with a completely self-consistent calculation for the collinear case with a scalar-relativistic pseudopotential (without SOC) to get the distribution of the spin moment and charge density in real space. Second, with the freezing potential of the electron density, SOC is managed as a nuisance in a non-self-consistent calculation using a fully-relativistic pseudopotential at different magnetization directions, i.e., each direction of magnetization is in-plane and perpendicular with the crystal plane.

The total energy from the simple force theorem is can be represented as [24],

$$E_{\mathrm{SDFT}}^{\mathrm{f},\hat{\mathrm{m}}} = \sum_{i}^{\mathrm{occ.}} \tilde{\varepsilon}_i^{\hat{\mathbf{m}}} + \Delta E[n, \mathbf{m}] + U, \quad (9)$$

$$E_{\mathrm{SDFT}}^{\mathrm{f},0} = \sum_{i}^{\mathrm{occ.}} \tilde{\varepsilon}_i^{0} + \Delta E[n, \mathbf{m}] + U, \quad (10)$$

$$\Delta E_{\mathrm{SDFT}}^{\mathrm{f},\hat{\mathbf{m}}} = E_{\mathrm{SDFT}}^{\mathrm{f},\hat{\mathbf{m}}} - E_{\mathrm{SDFT}}^{\mathrm{f},0} = \sum_{i}^{\mathrm{occ.}} \tilde{\varepsilon}_i^{\hat{\mathbf{m}}} - \sum_{i}^{\mathrm{occ.}} \tilde{\varepsilon}_i^{0} \,, \tag{11}$$

$$\tilde{E}_{\mathrm{SDFT}}^{\mathrm{f},\hat{\mathbf{m}}} = \sum_{i}^{\mathrm{occ.}} \tilde{\varepsilon}_i^{\hat{\mathbf{m}}} \,, \tag{12}$$

where $\tilde{E}_{\mathrm{SDFT}}^{\mathrm{f},\hat{\mathbf{m}}}$ represents the total energy difference by the system without SOC within the force theorem. $\Delta E[n,\mathbf{m}]$ participates of the spin density $\mathbf{m}(\mathbf{r})$ and electron density $n(\mathbf{r})$ that are persevering self-consistently without the potential of SOC. $\tilde{\varepsilon}_i^{\hat{\mathbf{m}}}$ and ε_i^0 indicates the eigenvalues for the potential ($\hat{V}_{\mathrm{eff}}$) with and without SOC, respectively.

The MCAE is estimated as the total energy deviation among the distinct direction of magnetizations. Give thought to the magnetization directions of $\hat{\mathbf{m}}_1$ and $\hat{\mathbf{m}}_2$, the MCAE is can be represented by [24],

$$\mathrm{MCAE} = \sum_{i}^{\mathrm{occ.}} \varepsilon_i^{\hat{\mathbf{m}}_1} - \sum_{i}^{\mathrm{occ.}} \varepsilon_i^{\hat{\mathbf{m}}_2} \,. \tag{13}$$

To detach the MCAE to the atom-resolved or **k**-resolved endowment, we examine the total energy of SDFT is can be represented by [24],

$$\tilde{E}_{\mathrm{SDFT}}^{\mathrm{gf},\hat{\mathbf{m}}} = \sum_{i} f_i^{\hat{\mathbf{m}}} (\tilde{\varepsilon}_i^{\hat{\mathbf{m}}} - \mu), \tag{14}$$

where $f_i^{\hat{\mathbf{m}}}$ are electron occupations with SOC, μ chemical potentials, and $\tilde{\varepsilon}_i^{\hat{\mathbf{m}}}$ eigenvalues for the potentials ($\hat{V}_{\mathrm{eff}}$) with SOC.

Using the explicit nation of $i = (\ell, \mathbf{k})$ [24],

$$\tilde{E}_{\mathrm{SDFT}}^{\mathrm{gf},\hat{\mathbf{m}}}(\mathbf{k}) = \sum_{\ell} f_{\ell\mathbf{k}}^{\hat{\mathbf{m}}} (\tilde{\varepsilon}_{\ell\mathbf{k}}^{\hat{\mathbf{m}}} - \mu), \tag{15}$$

$$\tilde{E}_{\mathrm{SDFT}}^{\mathrm{gf},\hat{\mathbf{m}}}(I) = \sum_{\ell}\sum_{\mathbf{k}}\sum_{\ell} f_{\ell\mathbf{k}}^{\hat{\mathbf{m}}} (\tilde{\varepsilon}_{\ell\mathbf{k}}^{\hat{\mathbf{m}}} - \mu) \left| \langle \chi_{Ia} | \Phi_{\ell\mathbf{k}} \rangle \right|^2 \tag{16}$$

$$\tilde{E}_{\mathrm{SDFT}}^{\mathrm{gf},\hat{\mathbf{m}}}(I,\mathbf{k}) = \sum_{\ell}\sum_{a} f_{\ell\mathbf{k}}^{\hat{\mathbf{m}}} \left(\tilde{\varepsilon}_{\ell\mathbf{k}}^{\hat{\mathbf{m}}} \right) \left| \langle \chi_{Ia} | \Phi_{\ell\mathbf{k}} \rangle \right|^2 \tag{17}$$

where the **k**-resolved or atom-resolved endowment hinges on $f_{\ell\mathbf{k}}^{\hat{\mathbf{m}}}$ and μ also $\tilde{\varepsilon}_{\ell\mathbf{k}}^{\hat{\mathbf{m}}}$. χ_{Ia} indicate the *a*'th atomic orbital on atom *I*. Both of them are the **k**-space distribution $\tilde{E}_{\mathrm{SDFT}}^{\mathrm{gf},\hat{\mathbf{m}}}(\mathbf{k})$ and the atomic distribution $\tilde{E}_{\mathrm{SDFT}}^{\mathrm{gf},\hat{\mathbf{m}}}(I)$ probably susceptible for μ. However, the primary characteristic of these distributions can get in $\tilde{\varepsilon}_{\ell\mathbf{k}}^{\hat{\mathbf{m}}}$. Accordingly, the **k**-space variation $\tilde{E}_{\mathrm{SDFT}}^{\mathrm{gf},\hat{\mathbf{m}}}(\mathbf{k})$ should have symmetries in the system.

In the GCFT approach, we can see the contribution of MCAE values from atom-resolved, **k**-resolved, and atomic **k**-resolved. Atom-resolved MCAE or **k**-resolved MCAE is specified from the total energy distinction among the [100] or [010] and [001] magnetization directions using the equation [24]:

$$\mathrm{MCAE}(I) = \delta\tilde{E}_{\mathrm{SDFT}}^{\mathrm{gf},[100]}(I) - \delta\tilde{E}_{\mathrm{SDFT}}^{\mathrm{gf},[001]}(I), \tag{18}$$

$$\mathrm{MCAE}(\mathbf{k}) = \delta\tilde{E}_{\mathrm{SDFT}}^{\mathrm{gf},[100]}(\mathbf{k}) - \delta\tilde{E}_{\mathrm{SDFT}}^{\mathrm{gf},[001]}(\mathbf{k}), \tag{19}$$

$$\mathrm{MCAE}(I,\mathbf{k}) = \delta\tilde{E}^{\mathrm{gf},[100]}_{\mathrm{SDFT}}(I,\mathbf{k}) - \delta\tilde{E}^{\mathrm{gf},[001]}_{\mathrm{SDFT}}(I,\mathbf{k}), \tag{20}$$

where I is atomic-resolved, **k** is **k**-resolved, and (l, **k**) is atomic orbital **k**-resolved. From the calculation of **k**-resolve MCAE, it can be shown that the contribution of positive and negative values is only observed in certain areas in the 2D first Brillouin zone [24]. Thus, the MCAE is negative or positive, indicating that the magnetization wick is easily perpendicular or in-plane with the crystal plane [11].

Perturbation Theory of Spin-Orbit Interaction

The spin-orbit Hamiltonian (H_{SOC}) is $\xi\mathbf{L}\cdot\mathbf{S}$. The $\mathbf{L}\cdot\mathbf{S}$ term may be described according to [21],

$$\mathbf{L}\cdot\mathbf{S} = \frac{1}{2}(L_+S_- + L_-S_+) + L_zS_z. \tag{21}$$

The z-component of the spin operator measures along the strength of the spin heading, thus [21],

$$S_z\left|\uparrow\right\rangle = +\frac{1}{2}\hbar\left|\uparrow\right\rangle \tag{22}$$

$$S_z\left|\downarrow\right\rangle = -\frac{1}{2}\hbar\left|\downarrow\right\rangle, \tag{23}$$

where $\left|\uparrow\right\rangle$ and $\left|\downarrow\right\rangle$ represent the eigenstates of the spin operator with spin orientations in the 'up' and 'down' directions, respectively.

In the case of the transition metal 3d-electron magnetism, the SOC constant, ξ, is less than 100 meV. This value is much smaller than the bandwidth (several eV). So, it can treat the SOC as a perturbation. Then, taking into account the perturbation theory, the shift in the worth of the Eigen energy E_n to the second-order term due to SOC is given by [21],

$$\delta E_n = \xi\left\langle n\left|\mathbf{L}\cdot\mathbf{S}\right|n\right\rangle + \xi^2\sum_{k\neq n}\frac{\left|\left\langle n\left|\mathbf{L}\cdot\mathbf{S}\right|k\right\rangle\right|^2}{E_n - E_k}, \tag{24}$$

where E_n and E_k are the corresponding Eigen energy values and $\left|n\right\rangle$ and $\left|k\right\rangle$ represent the eigenstates of the unperturbed Hamiltonian.

The unperturbed state has a well-defined spin character (in contrast to the perturbed ones) and is suitable for considering states such as [21],

$$\left|n\right\rangle = \sum_i c_{n,i}\left|\mathbf{k}, d_{n,i}, \sigma_n\right\rangle \tag{25}$$

where σ denotes spin, the index i runs over the d-orbitals ($d_{3z^2-r^2}, d_{xz}, d_{yz}, d_{xy}$, and $d_{x^2-y^2}$) and in the matter of the periodic tract, k denotes a point in the first Brillouin zone.

In the matter of robust exchange separation, the spin-up band is nearly completely filled, and empty entry states are included in the spin-down band. The only SOC among spin-up states will be considered. The contribution can be separated into two parts, that is, SOC

among parallel spin states and SOC among foreign spin states. The approximate MCAE of the SOC among the spin-up states can be given by [26],

$$\text{MCAE} \approx \xi^2 \sum_{\mathbf{k}_{o,u}} \frac{\left|\langle \mathbf{k}_o | \hat{l}_z | \mathbf{k}_u \rangle\right|^2 - \left|\langle \mathbf{k}_o | \hat{l}_x | \mathbf{k}_u \rangle\right|^2}{\varepsilon_{\mathbf{k}_u} - \varepsilon_{\mathbf{k}_o}}, \tag{26}$$

with $\varepsilon_{\mathbf{k}_u}$ and $\varepsilon_{\mathbf{k}_o}$ denote the energy of unoccupied and occupied states. $\mathbf{k}_u$ and $\mathbf{k}_o$ represent unoccupied and occupied states with $\hat{l}_z$, $\hat{l}_x$ the angular momentum operators and wave vectors $\mathbf{k}$. The SOC among the occupied and unoccupied states with the same (different) magnetic quantum number employing the operator $\hat{l}_z$ ($\hat{l}_x$ and $\hat{l}_y$) contributes positively (negatively) to MCAE [26][21]. The nonvanishing angular momentum matrix elements among the *d*-orbital states are listed in Table 1.

Table 1. Elements of the nonvanishing angular momentum matrix among *d*-orbital states [26].

Matrix elements	$\langle L_\sigma \rangle$ value
$\langle xz \vert L_z \vert yz \rangle$	1
$\langle x^2 - y^2 \vert L_z \vert xy \rangle$	2
$\langle z^2 \vert L_x \vert yz \rangle$	$\sqrt{3}$
$\langle xy \vert L_x \vert xz \rangle$	1
$\langle x^2 - y^2 \vert L_x \vert yz \rangle$	1
$\langle z^2 \vert L_y \vert xz \rangle$	$\sqrt{3}$
$\langle xy \vert L_y \vert yz \rangle$	1
$\langle x^2 - y^2 \vert L_y \vert xz \rangle$	1

Computational Details

The focus of this research is to examine the structure of the low-temperature rhombohedral of monolayer CrI_3, which has a Curie temperature of 61 K [28] and a monolayer CrI_3 of 45 K [9]. The experimental lattice parameters of the two-dimensional (2D) CrI_3 are $a = b = 6.859512$ Å, $c = 19.765290$ Å, $\alpha = \beta = 90°$, and $\gamma = 120$ ° [29]. The monolayer CrI_3 crystal structure consists of three atomic layers. The middle layer between the two iodine atom layers is a Cr atom layer, where the six nearest neighboring iodine atoms surround each Cr atom. The top view of the monolayer CrI_3 structure forms a honeycomb arrangement of Cr atoms. In addition, every Cr atom is encircled by six nearest neighbors I atoms, arranged in a side portion of the CrI_6 octahedral. An illustration of the crystal structure of the monolayer CrI_3 can be seen in Figure 1.

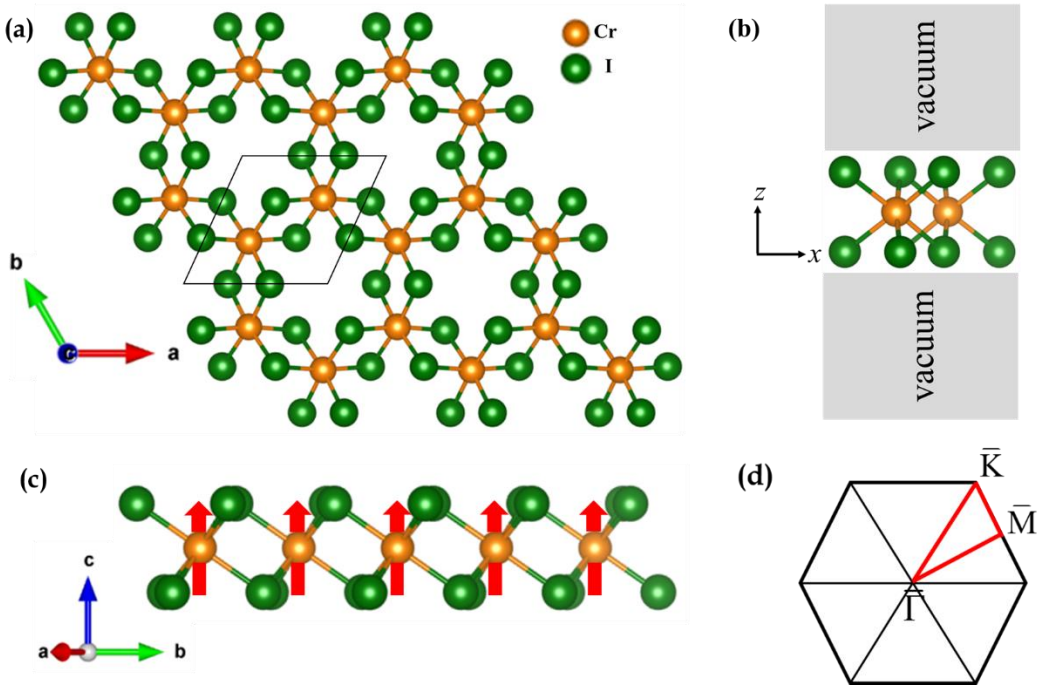

Figure 1. (a) Schematic illustration of the top view of the monolayer CrI_3 structure, forming a honeycomb arrangement. Chromium atoms are orange, while iodine atoms are green. The region bounded by the black line is the unit cell structure of the monolayer CrI_3. It consists of two Cr atoms and six I atoms. (b) Model structure of the monolayer CrI_3 for calculation. Both sides have a vacuum layer with a thickness of 17.96 Å. (c) Side view of the monolayer CrI_3 with the ferromagnetic configuration. (d) The 2D first Brillouin zone of the hexagonal lattice, the region bounded by the red line, is the irreducible region of the 2D first Brillouin zone [30].

In the calculation, we performed in CPVO code [17][18][19], which uses scalar and fully relativistic ultrasoft pseudopotentials and a plane waves basis [20][19]. In our calculation, use the SDFT scheme on the first-principles calculation with the Perdew-Burke-Ernzerhof (PBE) function in generalized gradient approximation (GGA) for the exchange-correlation energy [31] to investigate the electronic structure of the 2D monolayer ferromagnetic CrI_3. We make use of scalar relativistic calculations for the structural relaxation whilst retaining the in-plane lattice constant by making use of a $5\times5\times1$ **k**-mesh used in the first Brillouin zone sampling for monolayer CrI_3 [32]. An in-plane lattice constant of 6.85951 Å was used as the in-order value in the experiment [29]. The energy cut-offs of plane waves basis are 48 Ryd and 457 Ryd for the wave function and density, respectively [18]. We calculated MAE in 2D monolayer ferromagnetic CrI_3, which contribution from the MCAE originates from the SOC. We analyze the MCAE in both outlines. First, the MCAE is performed built on the TE distinct among the magnetization along the in-plane and perpendicular to the crystal plane. Second, the MCAE is performed on the basis of GCFT. In the GCFT scheme, we completed the atom-resolved, **k**-resolved, and atomic **k**-resolved contributions of the MCAE.

The experimental measurements show that CrI_3 is a ferromagnetic insulator with a relatively high Curie temperature of 61 K [28]. In 2017, 2D monolayer CrI_3 was successfully synthesized

in experiments. The experimental measurement results showed that the insulator is ferromagnetic by an easy-axis perpendicular to the crystal plane and a Curie temperature of 45 K [9]. Thus, the intrinsic ferromagnetic bulk of CrI_3 can be well maintained even though the layers are arranged up to the monolayer boundary. The results in this study indicate that the 2D monolayer CrI_3 is a ferromagnetic intrinsic magnetic material with an easy-axis perpendicular to the crystal plane. This is consistent with experimental measurements [9] and also the results of previous theoretical results [12]. The total magnetic moment of the monolayer CrI_3 is mainly contributed by Cr atoms, which is around 2.83 μ_B for each Cr atom. This is a good agreement with the experimental measurement of 3.0 μ_B [9] and as well with the previous theoretical results of 2.9 μ_B [33], 3.0 μ_B [12], 2.9 μ_B [34], and 3.1 μ_B [35].

Result and Discussion

Magnetic Anisotropy Energy on 2D Monolayer Ferromagnetic CrI_3

In this section, we will discuss more the magnetic properties of 2D monolayer ferromagnetic CrI_3. The calculations are carried out using first-principles calculations which use scalar-relativistic and fully relativistic pseudopotentials and plane waves basis, using GGA for the energy exchange-correlation function. In the calculation, MAE was evaluated by considering MCAE originating from SOC. The MCAE was calculated using the two methods of the TE difference and the GCFT. In the GCFT schema, we performed the atom-resolved, **k**-resolved, and atomic **k**-resolved contributions to the MCAE. We were using **k**-mesh 5×5×1 for MCAE calculations. In addition, in this study, the magnitude of the magnetic moment of each Cr atom was 2.83 μ_B, and the MCAE value of the 2D monolayer ferromagnetic CrI_3 was evaluated based on the calculation of TE and GCFT. The results are shown in Table 2. From Table 2, we can see that from the results of the MCAE calculation, there is a good agreement between those two methods. The positive MCAE indicates that the monolayer CrI_3 has an easy-axis perpendicular magnetic anisotropy to the crystal plane. This follows the previous experiment measurement [9] and the previous theoretical results. To match our results in detail with the previous theoretical and experimental ones, we summarized the lattice constant, magnetic moment, MCAE, and type of pseudopotential in Table 3.

Table 2. The MCAE value is calculated based on the TE, GCFT, and Bruno's formula.

Material	MCAE (TE) (meV/unit cell)	MCAE (GCFT) (meV/unit cell)	MCAE (Bruno's formula) (meV/unit cell)
monolayer CrI_3	1.72	1.75	0.28

Table 3. Comparison of MCAE values of 2D monolayer ferromagnetic CrI_3 with previous theoretical and experimental results. The lattice constant, magnetic moment of Cr atom, MCAE of 2D monolayer ferromagnetic CrI_3, and type of pseudopotential.

	Reference	a (Å)	m_{Cr} (μ_B)	MCAE	Type of pseudopotential
Experiment	Huang et al. (2017)	6.873	3.00	easy-axis anisotropy, perpendicular to the crystal plane	-
	Patil et al. (2019)	6.859	-	-	-
Computational calculation	W. Zhang et al. (2015)	7.006	3.00	685.5 μeV/Cr	PAW: GGA-PBE
	Lado & Rossier (2017)	-	3.00	0.65 meV	PAW: PBE
	Guo et al. (2018)	6.867	2.93	0.79 meV	all-electron FP-LAPW: GGA-PBE
	Webster & Yan al. (2018)	7.008	3.00	803.65 μeV/Cr	PAW: GGA-PBE
	Jiang et al. (2018)	-	-	0.9 meV/Cr	-
	C. Huang et al. (2018)	-	-	1.5 meV/unit cell	GGA-PBE
	Pei at al. (2019)	7.000	3.00	737 μeV/f.u.	GGA-PBE
	Gudelli at al. (2019)	6.867	3.20	0.678 meV/fu	PAW: GGA+U-PBE
	Pizzochero et al. (2020)	-	3.00	0.39; 0.90; and 0.70 meV	GGA-PBE; meta GGA-SCAN; dan hybrid Fock-exchange/density -functionals-HSE06
	Xu et al. (2020)	7.006	3.10	0.990 meV/Cr	PAW: GGA-PBE
	Zhao et al. (2021)	6.982	-	0.6 meV/f.u.	PAW: HSE06+SOC
	This work	6.859	2.83	1.7 meV/unit cell	GGA-PBE

Furthermore, in calculating the MCAE using the GCFT method, we performed a calculation of the MCAE values of atom-resolved, **k**-resolved, and atomic **k**-resolved. The results of the MCAE values of atom-resolved can be seen in Figure 2, where a positive value indicates that the perpendicular MCAE and the negative indicates the in-plane MCAE. We can see that from Figure 2 shows the contribution of the primary positive MCAE value from the Cr atom. In addition, in the 2D monolayer ferromagnetic CrI_3, the I atom also contributes to perpendicular MCAE.

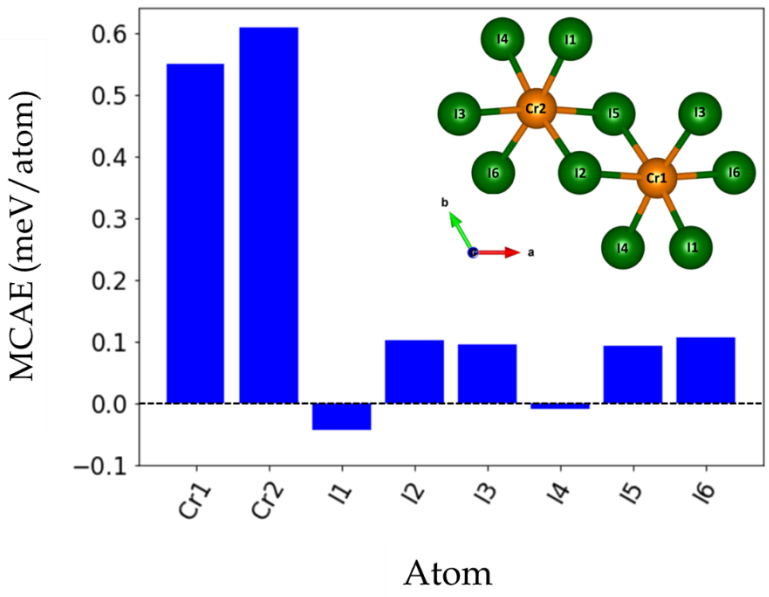

Figure 2. Atom-resolved MCAE 2D monolayer ferromagnetic CrI_3.

To elucidate more about the origin of the positive value of MCAE in 2D monolayer ferromagnetic CrI_3, we calculated the **k**-resolved MCAE and atomic **k**-resolved MCAE in the 2D Brillouin zone for each Cr and I atom system. The results are shown in Figure 3 and Figure 4, respectively. The energy ranges from red to blue, indicating positive to negative contribution to the MCAE. We can see that, in the 2D Brillouin zone, only certain regions contribute to MCAE (other regions are almost absent). From this **k**-resolved MCAE, it can be found that only certain regions in the 2D Brillouin zone contribute to positive and negative MCAE.

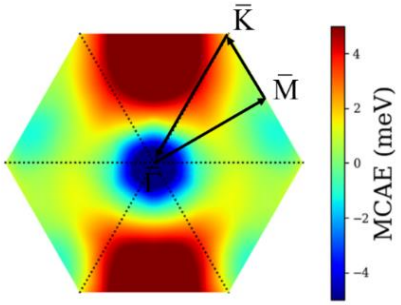

Figure 3. k-resolved MCAE 2D monolayer ferromagnetic CrI_3.

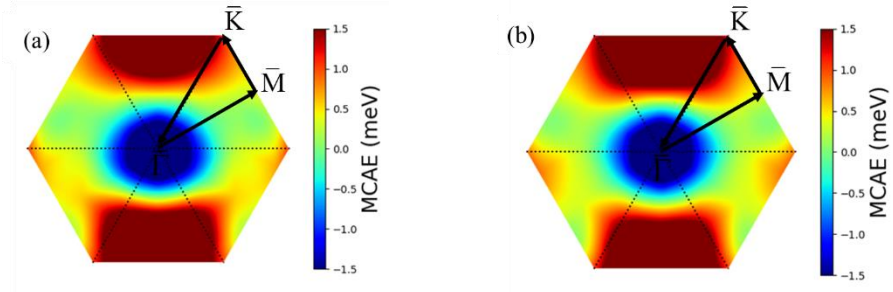

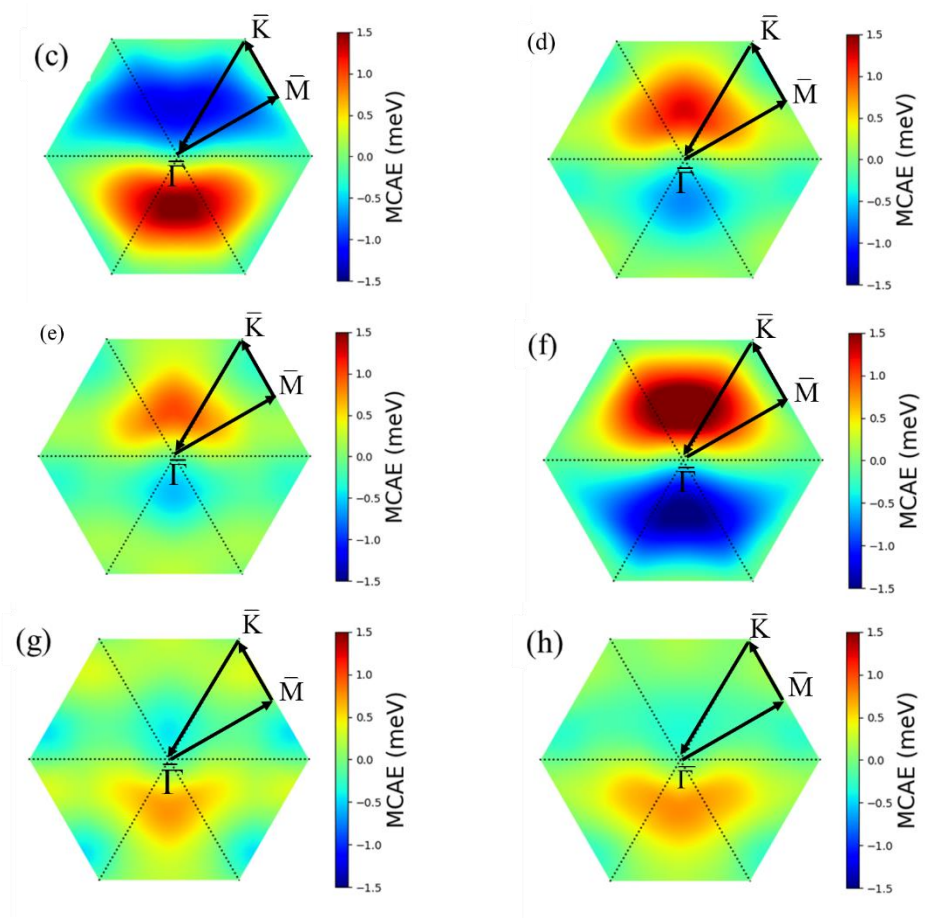

Figure 4. Atomic **k**-resolved MCAE 2D monolayer ferromagnetic CrI_3, (a) Cr (1) atom, (b) Cr (2) atom, (c) I (1) atom, (d) I (2) atom, (e) I (3) atom, (f) I (4) atom, (g) I (5) atom, and (h) I (6) atom.

Next, we calculated the MCAE 2D monolayer ferromagnetic CrI_3 by using Bruno's formula. MCAE is proportional to the orbital moment as in Bruno's formula $\mathrm{MCAE} = \xi \Delta m_o / 4\mu_B$, where $\Delta m_o = m_o[001] - m_o[100]$ (the difference between the perpendicular and in-plane orbital moments), μ_B is Bohr magneton and ξ is the SOC constant [36]. The values of orbital moments are reported both for [100] and [001] directions, and the result of an orbital moment for the Cr atom and I atom are shown in Figure 5 (a). These orbital moment values are a good agreement with previous theoretical results [37]. Therefore, we can estimate the MCAE using Bruno's formula by the results of the orbital moment. We used the SOC constants of 58 meV for the Cr atom in our calculations for Bruno's formula. The MCAE results for monolayer CrI_3 are shown in Table 3. The atom-resolved MCAE values from Bruno's formula on monolayer CrI_3 can be seen in Figure 5 (b), where a positive value indicates the perpendicular MCAE and a negative indicates the in-plane MCAE.

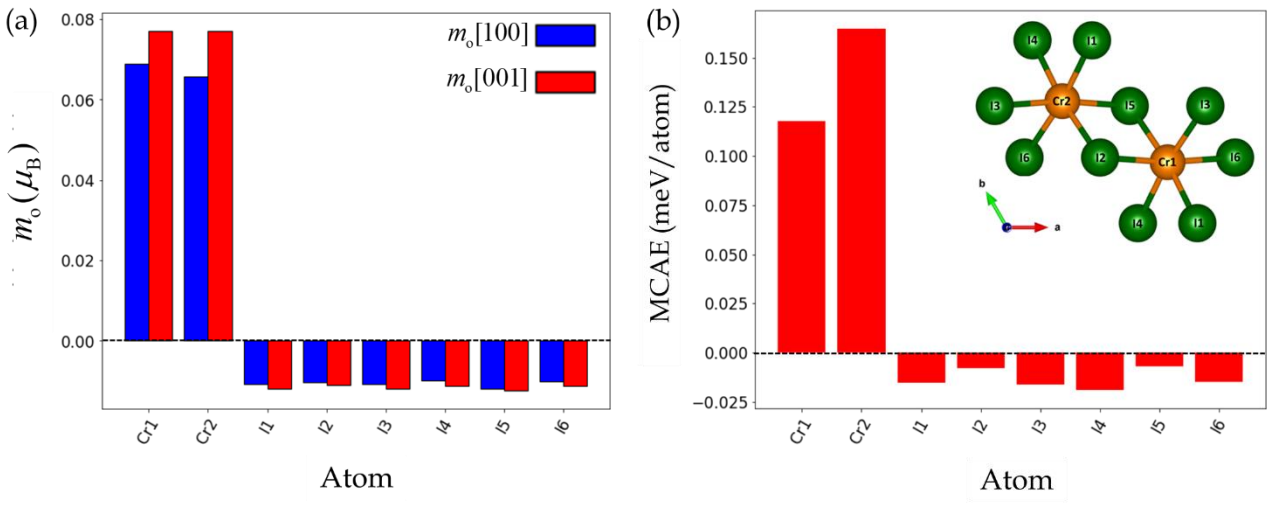

Figure 5. (a) Orbital magnetic moment (m_0) for each Cr and I atom in monolayer CrI_3. (b) Atom-resolved MCAE from Bruno's formula for 2D monolayer ferromagnetic CrI_3.

In order to explain the possible origin of the PMA, we investigated the band-filling effect for 2D monolayer ferromagnetic CrI_3. The band-filling effect here refers to the changes in the Fermi level by reducing or increasing the number of valence electrons per unit cell. This estimation was finished by making use of the data of GCFT. The result can be seen in Figure 6. The band-filling effect here refers to the changes in the Fermi level by reducing or increasing the number of valence electrons. From the figure, we can see that MCAE behavior is dependent on band-filling. In the 2D monolayer ferromagnetic CrI_3, the actual Fermi energy area is not the top of MCAE. It shows that we could more distant increase the MCAE by changing the position of the Fermi energy.

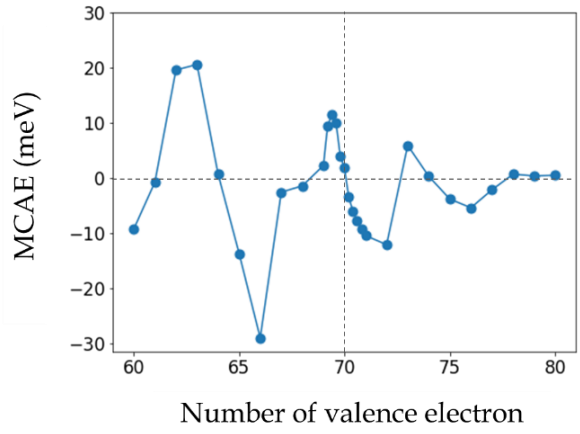

Figure 6. MCAE is a function of the number of valence electrons. Vertical dotted lines indicate the actual number of valence electrons in the unit cell.

The contribution to the positive and negative MCAE can be attributed to certain coupling pairs in the states above and below the Fermi energy by considering the second-order perturbation theory, where in states near the Fermi energy, it is important to discuss the origin of MCAE. To examine the details of the coupling pair near the Fermi energy, we plotted the band structure curves of the 3*d* orbitals for each Cr atom and as shown in Figure 10. Based on the analysis of the perturbation theory in equation (26) in the Theoretical Framework Section, here we focus on the contributing states of the Cr-3*d* orbitals in the spin-up section, because the majority of the spin-up areas of the Cr-3*d* orbitals are completely filled with spin-states in the occupied states and unoccupied states. This is different from the endowment states of the Cr-3*d* orbital in the spin-down area, where the majority of the spin-down area of the Cr-3*d* orbital is completely filled in the unoccupied state region, so that is less significant to determine the positive and negative contribution of MCAE values in the 2D Brillouin zone for the 2D monolayer ferromagnetic CrI_3 due to the SOC of the *d*-orbital states in the spin-down states (see Figure 9).

Table 4. Positive and negative contributions to the MCAE values in the first 2D Brillouin zone for the 2D monolayer ferromagnetic CrI_3 due to the SOC of the *d*-orbital states. *o* is an occupied state and *u* is an unoccupied state.

Line in first Brillouin zone	Matrix elements
$\bar{\Gamma}-1/4\bar{\Gamma}\bar{\mathrm{M}}$	$\langle o, xz \vert \hat{l}_z \vert u, yz \rangle$
	$\langle o, x^2-y^2 \vert \hat{l}_z \vert u, xy \rangle$
	$\langle o, xy \vert \hat{l}_x \vert u, xz \rangle$
	$\langle o, x^2-y^2 \vert \hat{l}_x \vert u, yz \rangle$
	$\langle o, 3z^2-r^2 \vert \hat{l}_x \vert u, yz \rangle$
$\bar{\mathrm{M}}-\bar{\mathrm{K}}$	$\langle o, x^2-y^2 \vert \hat{l}_z \vert u, xy \rangle$
	$\langle o, xy \vert \hat{l}_x \vert u, xz \rangle$
	$\langle o, x^2-y^2 \vert \hat{l}_x \vert u, yz \rangle$
	$\langle o, 3z^2-r^2 \vert \hat{l}_x \vert u, yz \rangle$
$\bar{\mathrm{K}}-3/4\bar{\mathrm{K}}\bar{\Gamma}$	$\langle o, xz \vert \hat{l}_z \vert u, yz \rangle$
	$\langle o, x^2-y^2 \vert \hat{l}_z \vert u, xy \rangle$
	$\langle o, xy \vert \hat{l}_x \vert u, xz \rangle$
	$\langle o, x^2-y^2 \vert \hat{l}_x \vert u, yz \rangle$
	$\langle o, 3z^2-r^2 \vert \hat{l}_x \vert u, yz \rangle$

Furthermore, from these **k**-resolved MCAE results, we can clearly see the region in the 2D first Brillouin zone that contributes to positive or negative MCAE. Based on the analysis in Table 1 in the Theoretical Framework section, we summarize a list of possible *d*-orbital coupling pairs near the Fermi energy, as shown in Table 4. From Table 4, we can see that the results of **k**-resolved MCAE in the area in the first 2D Brillouin zone that contribute to negative MCAE is greater

than the contribution of positive MCAE in each line $\bar{\Gamma}-1/4\bar{\Gamma}\bar{M}$, $\bar{M}-\bar{K}$, and $\bar{K}-3/4\bar{K}\bar{\Gamma}$. At the line $\bar{\Gamma}-1/4\bar{\Gamma}\bar{M}$, the contribution of the negative MCAE is 3.7, and the contribution of the positive MCAE is 3. At the line $\bar{M}-\bar{K}$, the contribution of the negative MCAE is 3.7, and the contribution of the positive MCAE is 2. At the line $\bar{K}-3/4\bar{K}\bar{\Gamma}$, the contribution from the negative MCAE is 3.7, and the contribution from the positive MCAE is 3. This is not in accordance with the results of **k**-resolved MCAE obtained in Figure 3, where the line $\bar{K}-3/4\bar{K}\bar{\Gamma}$ contributes positive MCAE, so to explain, it is necessary to include spin-flip interactions [26] to determine the possible coupling pair contributions.

Electronic Structures and Optical Properties on 2D Monolayer Ferromagnetic CrI_3

In this section, we will further discuss the density of state (DOS), band structure, and optical properties of 2D monolayer ferromagnetic CrI_3. The results of the DOS curve it is shown in Figure 7 and Figure 8 for the *d*-orbital on the Cr atom and the *p*-orbital on the I atom, respectively. Based on the results of the DOS curve in Figure 7 and Figure 8 show that in the near Fermi level, the conduction band is dominated by the weakly hybridized state of Cr-3*d* with the I-5*p* state for both spin directions, and the valence band state in the spin-down direction is dominated I-5*p* orbitals. More interestingly, the Cr-3*d* orbital in the occupied state is overlooked in the spin-up direction, and the spin-down Cr-3*d* orbital is completely in the unoccupied state. This is also consistent with the previous theoretical results [38].

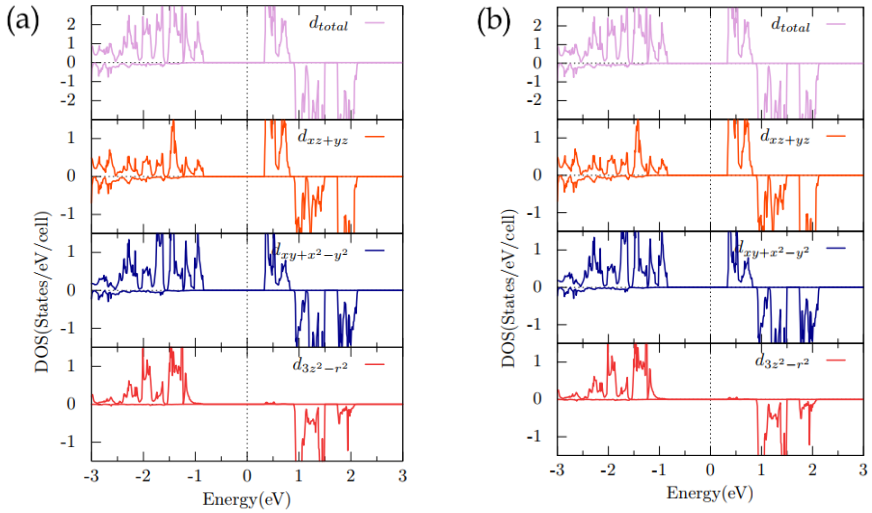

Figure 7. Total and partial density of state of the 2D monolayer ferromagnetic CrI_3 of the *d*-orbitals on the Cr atom for (a) Cr (1) atom and (b) Cr (2) atom.

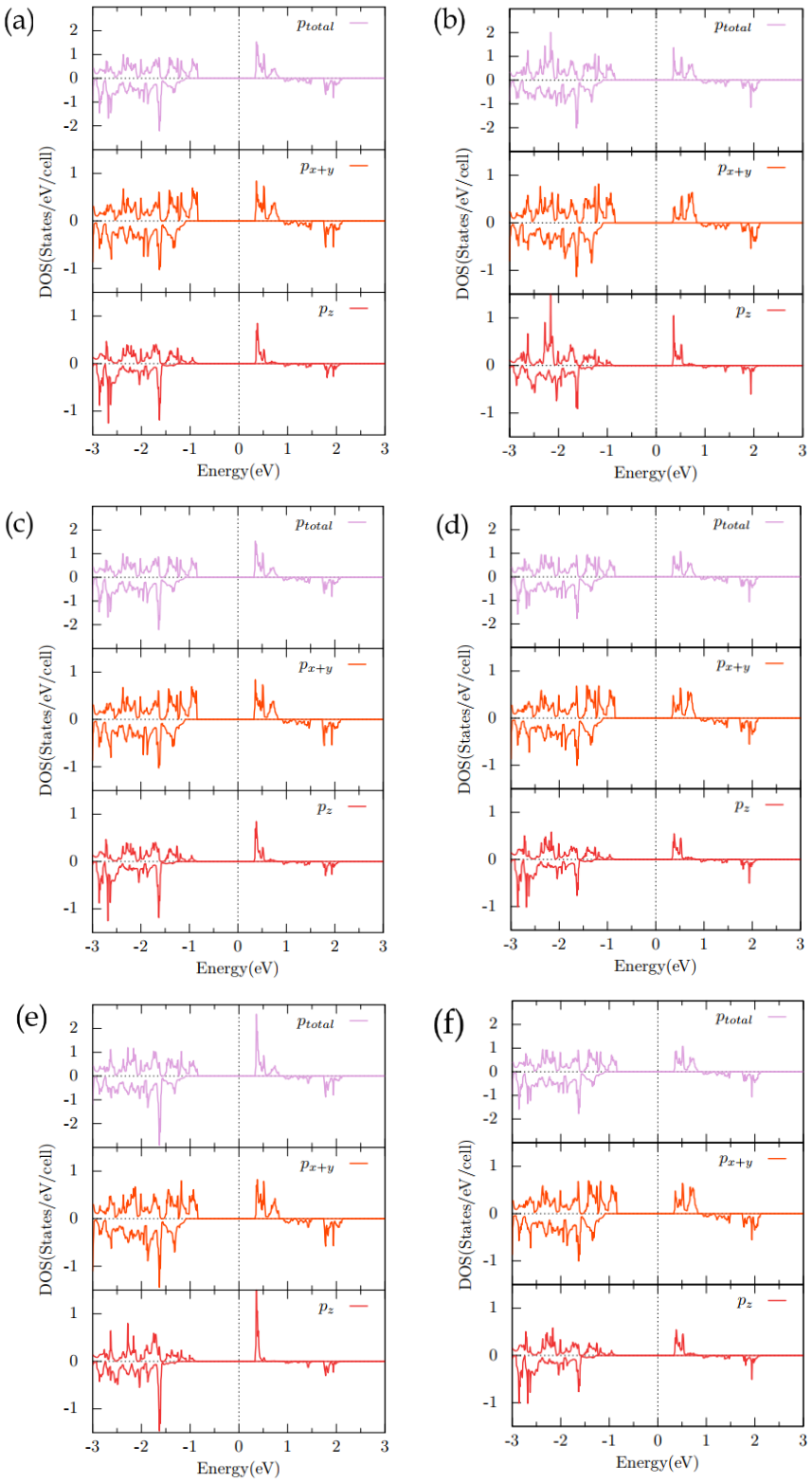

Figure 8. Total and partial density of state of the 2D monolayer ferromagnetic CrI_3 of the *p*-orbitals on I atom for (a) I (1) atom, (b) I (2) atom, (c) I (3) atom, (d) I (4) atom, (e) I (5) atom, and (f) I (6) atom.

In this study, we found that in the DOS curve, which is shown in Figure 7 and Figure 8. At the near Fermi level, in the Cr-3*d* atom state with the I-5*p* atom state, the spin-up conduction band is dominated. On the other hand, in the Cr-3*d* atom state, the spin-down conduction band is primarily filled. Furthermore, the spin-up valence band is contributed from the state of the Cr-3*d* atom with the combination of the I-5*p*, and the I-5*p* atom, mainly contributing to the spin-down valence band. This result is also consistent with previous theoretical results [33]. In addition, hybridization among the Cr-3*d* and I-5*p* orbitals confirms the superexchange interaction among the Cr-3*d* orbitals and the neighboring I-5*p* orbitals [38].

Next, we found that from the band structure, 2D monolayer CrI_3 has a spin-up band gap energy value of 1.21 eV and a spin-down band gap energy value of 1.99 eV, this is consistent with the previous theoretical result, and the summary results can be seen in Table 5. The band gap energy value is obtained from the difference in the energy value between the maximum valence band energy value and the minimum conduction band energy value [39]. The maximum valence band is contributed by the I atom of the *px*, *py*, and *pz* states and the combination of the *d*-orbital states of the Cr atom. In contrast, the minimum conduction band is contributed by the *d*-orbital state of the Cr atom and the combination of the *p*-orbital states of the I atom.

Table 5. Comparison of the band gap energy value of the 2D monolayer ferromagnetic CrI_3 with the previous theoretical result. The lattice constant, magnetic moment of Cr atom, band gap energy of 2D monolayer ferromagnetic CrI_3, and type of pseudopotential.

Reference	a (Å)	m_{Cr} (μ_B)	band gap (eV)	Type of pseudopotential
J. Liu et al. (2015)	7.079	3.44	1.09	PAW: GGA-PBE
Wei-Bing Zhang et al. (2015)	7.006	3.00	1.143 (spin-up); 2.109 (spin-down)	PAW: GGA-PBE
Hongbo Wang et al. (2016)	7.000	-	1.1	PAW: GGA-PBE
Guanxing Guo et al. (2018)	6.867	2.93	1.23 (spin-up); 1.90 (spin-down)	All electron FP-LAPW: GGA-PBE
Lucas Webster et al. (2018)	7.008	3.00	0.89	PAW: GGA-PBE
Zheng et al. (2018)	7.000	-	0.88	PAW: GGA-PBE
Jiayong Zhang et al. (2018)	7.000	3.00	1.19	GGA-PBE
Aroop K. Behera et al. (2019)	6.963	3.00	0.8	GGA+U-PBEsol
Zewen Wu et al. (2019)	6.978	-	1.124 (spin-up); 2.169 (spin-down)	PBE-GGA
Vijay Kumar Gudell et al. (2019)	6.867	3.20	0.81	PAW: GGA+U-PBE
Qin-Fang Xu et al. (2020)	7.006	3.10	1.18	PAW: GGA-PBE
This work	6.859	2.83	1.21 (spin-up); 1.99 (spin-down)	GGA-PBE

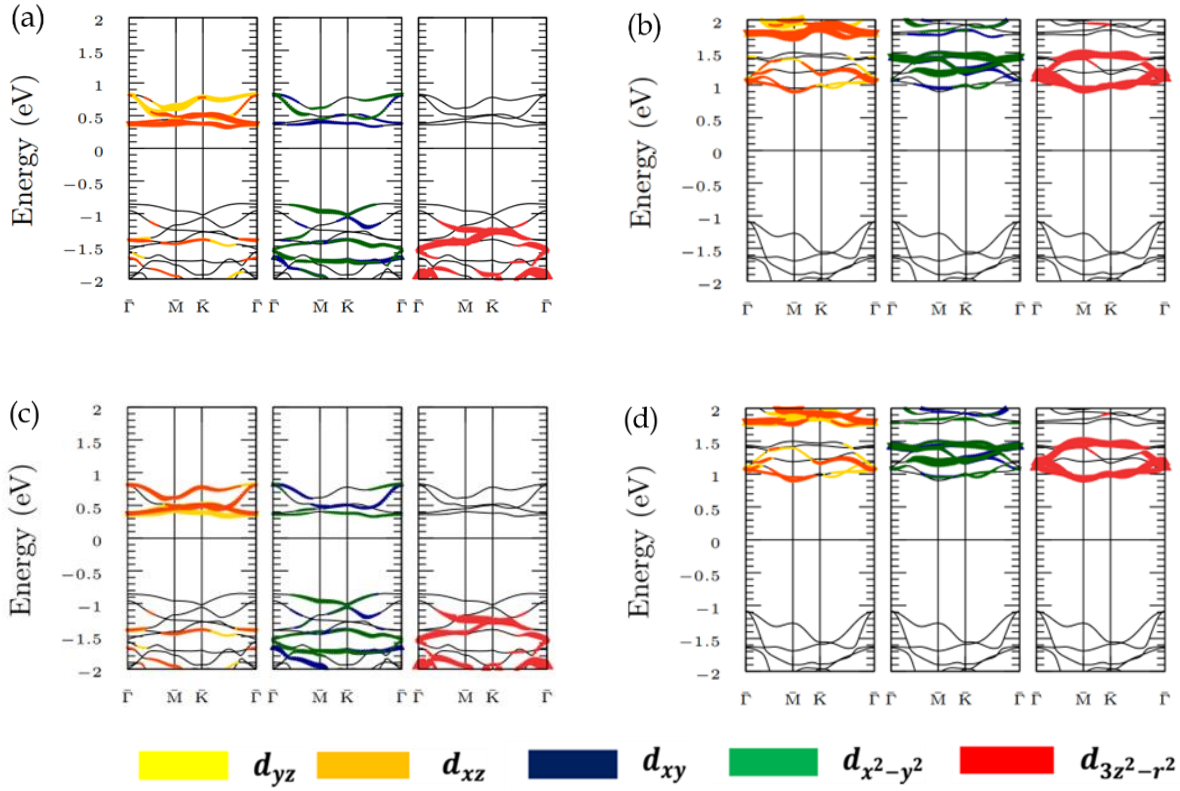

Figure 9. Electronic structure of 2D monolayer ferromagnetic CrI_3 from the *d*-orbitals on the Cr atom for (a) spin-up Cr (1), (b) spin-down Cr (1), (c) spin-up Cr (2), (d) spin-down Cr (2). The main components of the Cr 3*d* orbital ($d_{yz}, d_{xz}, d_{x^2-y^2}, d_{xy}$, and $d_{3z^2-r^2}$), for spin-states filled with, d_{yz} are marked in red-orange, d_{xz} are marked in gold color, $d_{x^2-y^2}$ are marked in dark green, d_{xy} are marked in dark blue, and $d_{3z^2-r^2}$ are marked in red. The color of the bar indicates the type of orbital.

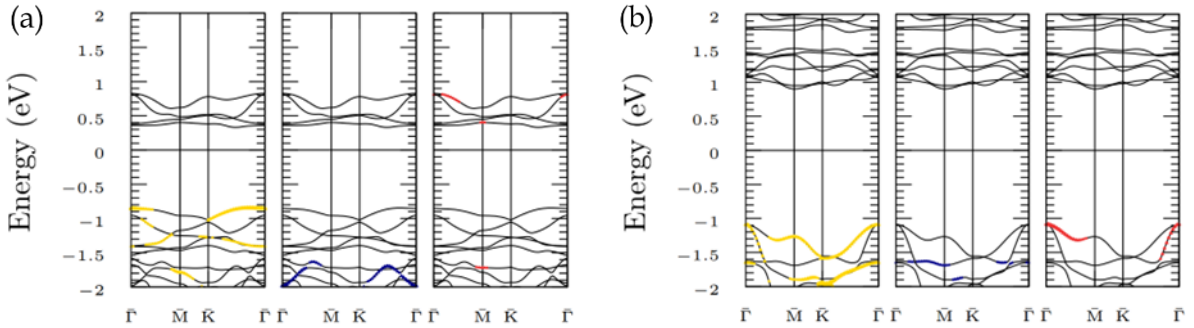

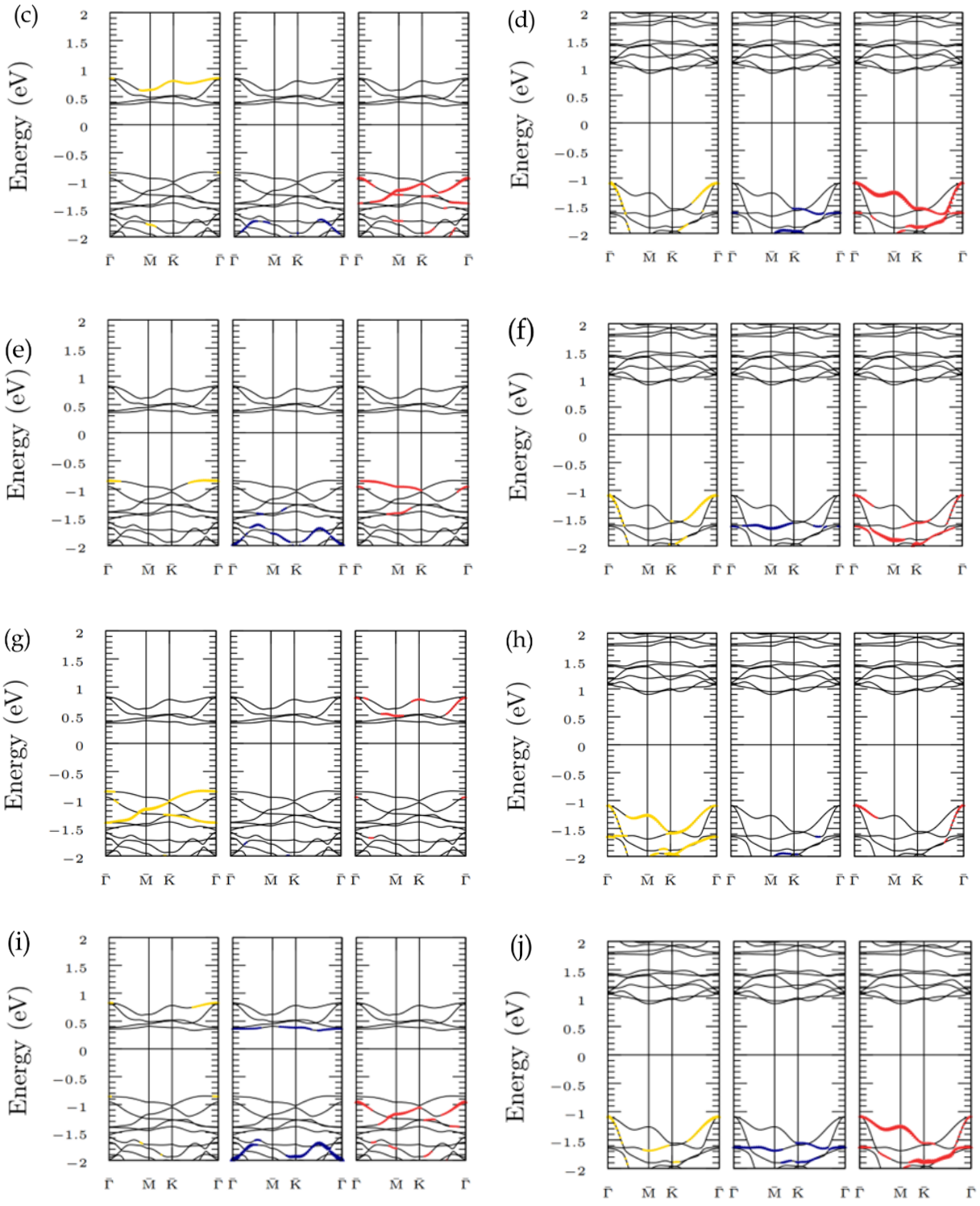
(c)
(d)
(e)
(f)
(g)
(h)
(i)
(j)
Energy (eV)
2
1.5
1
0.5
0
−0.5
−1
−1.5
−2
Γ̄ M̄ K̄ Γ̄ Γ̄ M̄ K̄ Γ̄ Γ̄ M̄ K̄ Γ̄

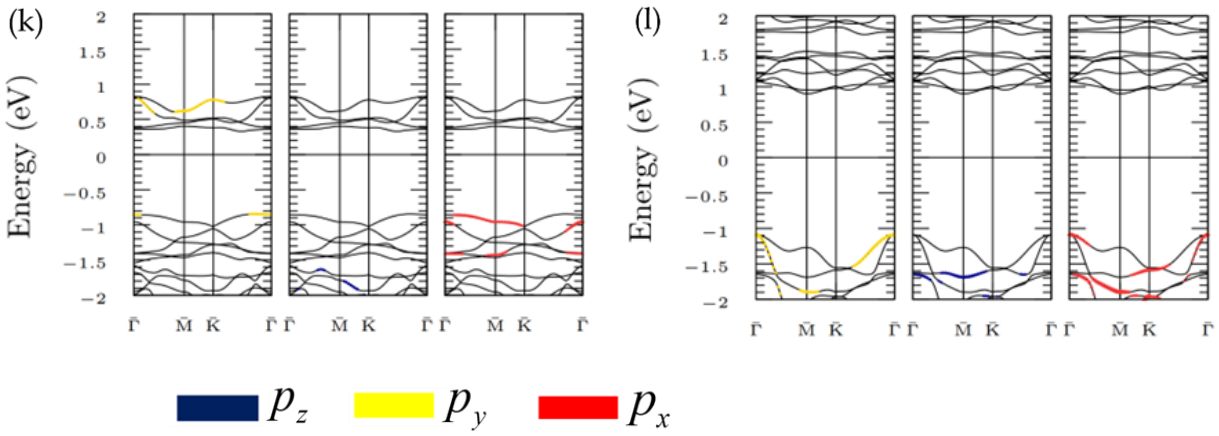

Figure 10. Electronic structure of 2D monolayer ferromagnetic CrI_3 from *p*-orbitals on the I atom for (a) spin-up I (1), (b) spin-down I (1), (c) spin-up I (2), (d) spin-down I (2), (e) spin-up I (3), (f) spin-down I (3), (g) spin-up I (4), (h) spin-down I (4), (i) spin-up I (5), (j) spin-down I (5), (k) spin-up I (6), dan (l) spin-down I (6). The dominant components in the I-5*p* orbitals are p_x, p_y, and p_z, for spin-states filled with P_y are marked in gold, p_z is marked in dark blue, p_x is in red. The color of the bar indicates the type of orbital.

Conclusion

In summary, the focus of this research has been on the investigation of magnetic properties, such as MAE, built on the SDFT scheme. We discussed the details of the MCAE on the 2D monolayer ferromagnetic CrI_3. In the calculation, we considered that the contribution to the MAE part is performed by the MCAE originating from the SOC. The MCAE part was calculated on the basis of the TE and the GCFT. From the GCFT schema, we performed the atom-resolved, **k**-resolved, and atomic **k**-resolved contributions to the MCAEs. For comparison, we add the results of previous theoretical and experimental measurements of a 2D monolayer CrI_3 ferromagnetic in the results of the section Magnetic Anisotropy on 2D Monolayer Ferromagnetic CrI_3. From the MCAE calculations based on the TE and GCFT, confirming that it has a good agreement value, the results are shown in the section Magnetic Anisotropy on 2D Monolayer Ferromagnetic CrI_3. This agreement makes it possible to carry out further analyzes of atom-resolved MCAE and **k**-resolved MCAE on 2D monolayer ferromagnetic CrI_3. Atom-resolved MCAE shows that the primary positive contribution to MCAE gets in from the Cr atom. Furthermore, by the results of **k**-resolved MCAE, we can clear that the region in the 2D first Brillouin zone that contributes to MCAE is positive or negative. The negative MCAE contribution is at $\bar{\Gamma}$ points, and the positive MCAE is mainly placed at the line $\bar{K}-3/4\bar{K}\bar{\Gamma}$ in the 2D first Brillouin zone. Based on the analysis in the section Theoretical Framework, the authors summarize a list of possible *d*-orbital pairs close by the Fermi energy, as shown in the section Magnetic Anisotropy on 2D monolayer ferromagnetic CrI_3. In the GCFT scheme, we can clarify the possible origin in terms of the details of the electronic structure. In addition, on the basis of the GCFT method, other emerging phenomena at the ferromagnetic/oxide interface, such as the Rashba effect, are possible to investigate, which may be calculated in future research. The Rashba effect at the interface is responsible for producing an effective field for the magnetization switching in

spin-transfer-torque MRAM devices [40][41] and spin-to-charge conversion [42]. Our systematic calculation in this work may also help design an effective structure of monolayer CrI_3 systems in new 2D material as a magnetic electrode in MRAM or 2D material in magnetic sensor and spintronic device designs.

Acknowledgment

The authors thank Laboratory Theoretical and Computational Nanoscience, Division of Mathematical and Physical Science, Kanazawa University, Japan. We performed using the facilities of the cluster computer (mic) 4 cores for the first-principles calculations, Division of Mathematical and Physical Science, Kanazawa University, Japan.

References

[1] A. Agrawal and A. Choudhary, "Perspective : Materials informatics and big data : Realization of the 'fourth paradigm' of science in materials science," *APL Mater.*, vol. 053208, no. April 2016, 2018, doi: 10.1063/1.4946894.

[2] G. R. Schleder, A. C. M. Padilha, C. M. Acosta, and M. Costa, "From DFT to machine learning : recent approaches to materials science-a review," *JPhys Mater.*, pp. 0–46, 2019.

[3] C. Chen, Y. Zuo, W. Ye, X. Li, and S. P. Ong, "Learning properties of ordered and disordered materials from multi-fidelity data," *Nat. Comput. Sci.*, vol. 1, no. January, 2021, doi: 10.1038/s43588-020-00002-x.

[4] B. Dieny and M. Chshiev, "Perpendicular magnetic anisotropy at transition metal/oxide interfaces and applications," *Rev. Mod. Phys.*, vol. 89, no. 2, pp. 025008–025062, 2017, doi: 10.1103/RevModPhys.89.025008.

[5] S. Haastrup, M. Strange, M. Pandey, T. Deilmann, and P. S. Schmidt, "The Computational 2D Materials Database : high-throughput modeling and discovery of atomically thin crystals," *2D Mater.*, 2018, doi: 10.1088/2053-1583/aacfc1.

[6] H. Yang *et al.*, "Two-dimensional materials prospects for non-volatile spintronic memories," *Nature*, vol. 606, no. 7915, pp. 663–673, 2022, doi: 10.1038/s41586-022-04768-0.

[7] C. Tang, K. Ostrikov, S. Sanvito, and A. Du, "Prediction of room-temperature ferromagnetism and large perpendicular magnetic anisotropy in a planar hypercoordinate FeB_3 monolayer," *Nanoscale Horizons*, vol. 6, no. 1, pp. 43–48, 2021, doi: 10.1039/d0nh00598c.

[8] R. Han, Z. Jiang, and Y. Yan, "Prediction of Novel 2D Intrinsic Ferromagnetic Materials with High Curie Temperature and Large Perpendicular Magnetic Anisotropy," *Phys. Chem.*, pp. 1–9, 2020, doi: 10.1021/acs.jpcc.0c01307.

[9] B. Huang *et al.*, "Layer-dependent ferromagnetism in a van der Waals crystal down to the monolayer limit," *Nat. Publ. Gr.*, vol. 546, no. 7657, pp. 270–273, 2017, doi: 10.1038/nature22391.

[10] C. Gong *et al.*, "Discovery of intrinsic ferromagnetism in two-dimensional van der Waals crystals," *Nat. Publ. Gr.*, vol. 546, no. 7657, pp. 265–269, 2017, doi: 10.1038/nature22060.

[11] Q. Pei, B. Zhou, W. Mi, and Y. Cheng, "Triferroic Material and Electrical Control of Valley Degree of Freedom," *ACS Appl. Mater. Interfaces*, 2019, doi: 10.1021/acsami.9b02095.

[12] J. L. Lado and J. F. Rossier, "On the origin of magnetic anisotropy in two dimensional CrI_3," *2D Mater.*, vol. 4, pp. 035002–035012, 2017, doi: https://doi.org/10.1088/2053-1583/aa75ed.

[13] L. Chen *et al.*, "Magnetic anisotropy in ferromagnetic CrI_3," *Phys. Rev. B 101*, vol. 134418, pp. 1–8, 2020, doi: 10.1103/PhysRevB.101.134418.

[14] J. Kim *et al.*, "Exploitable Magnetic Anisotropy of the Two-Dimensional Magnet CrI_3," *Nano Lett.*, vol. 20, pp. 929–935, 2020, doi: 10.1021/acs.nanolett.9b03815.

[15] P. V. Ong, N. Kioussis, P. K. Amiri, and K. L. Wang, "Electric-field-driven magnetization switching and nonlinear magnetoelasticity in Au/FeCo/MgO heterostructures," *Sci. Rep.*, vol. 6, no. June, pp. 1–8, 2016, doi: 10.1038/srep29815.

[16] I. Pardede, D. Yoshikawa, T. Kanagawa, N. Ikhsan, M. Obata, and T. Oda, "Anatomy of magnetic anisotropy and voltage-controlled magnetic anisotropy in metal oxide heterostructure from first principles," *Crystals*, vol. 10, no. 12, pp. 1–17, 2020, doi: 10.3390/cryst10121118.

[17] K. Laasonen, "Ab Initio Molecular Dynamics for d-Electron Systems : Liquid Copper at 1500 K," vol. 69, no. 13, pp. 1982–1985, 1992, doi: doi.org/10.1103/PhysRevLett.69.1982.

[18] K. Laasonen, A. Pasquarello, R. Car, C. Lee, and D. Vanderbilt, "Car-Parrinello molecular dynamics with Vanderbilt ultrasoft pseudopotentials," *Phys. Rev. B*, vol. 47, no. 16, pp. 10142–10153, 1993, doi: 10.1103/PhysRevB.47.10142.

[19] T. Oda, A. Pasquarello, and R. Car, "Fully Unconstrained Approach to Noncollinear Magnetism: Application to Small Fe Clusters," *Phys. Rev. Latters*, vol. 80, pp. 18–21, 1998, doi: doi.org/10.1103/PhysRevLett.80.3622.

[20] T. Oda and A. Hosokawa, "Fully relativistic two-component-spinor approach in the ultrasoft-pseudopotential plane-wave method," *Phys. Rev. B - Condens. Matter Mater. Phys.*, vol. 72, no. 22, pp. 1–4, 2005, doi: 10.1103/PhysRevB.72.224428.

[21] J. Kubler, *Theory of Itenerant Electron Magnetism*. New York: Oxford University Press, 2009.

[22] P. Hohenberg and W. Kohn, "Inhomogeneous Electron Gas*," *Phys. Rev.*, vol. 136, 1964, doi: 10.1103/PhysRev.136.B864.

[23] W. Kohn and L. J. Sham, "Self-Consistent Equations Including Exchange and Correlation Effects*," *Phys. Rev.*, vol. 140, 1965, doi: 10.1103/PhysRev.140.A1133.

[24] I. Pardede *et al.*, "Anatomy of large perpendicular magnetic anisotropy in free-standing Co/Ni (1 1 1) multilayer," *J. Magn. Magn. Mater.*, vol. 500, no. November 2019, p. 166357, 2020, doi: 10.1016/j.jmmm.2019.166357.

[25] A. G. H. O. Daalderop, P. J. Kelly and M. F. H. Schuurmans, "First-principles calculation of the magnetocrystalline of iron, cobalt, anti nickel," *Phys. Rev. B*, vol. 41, no. 17, pp. 11919–11937, 1990, doi: https://doi.org/10.1103/PhysRevB.41.11919.

[26] D. Wang, R. Wu, and A. J. Freeman, "First-principles theory of surface magnetocrystalline anisotropy and the diatomic-pair model," *Phys. Rev. B*, vol. 47, no. 22, pp. 932–947, 1993, doi: 10.1103/PhysRevB.47.14932.

[27] D. Li, A. Smogunov, C. Barreteau, F. Ducastelle, and D. Spanjaard, "Magnetocrystalline anisotropy energy of Fe (001) and Fe (110) slabs and nanoclusters: A detailed local analysis within a tight-binding model," *Phys. Rev. B - Condens. Matter Mater. Phys.*, vol. 88, no. 21, pp. 1–9, 2013, doi: 10.1103/PhysRevB.88.214413.

[28] M. A. McGuire, H. Dixit, V. R. Cooper, and B. C. Sales, "Coupling of crystal structure and magnetism in the layered, ferromagnetic insulator CrI_3," *Chem. Mater.*, vol. 27, no. 2, pp. 612–620, 2015, doi: 10.1021/cm504242t.

[29] R. A. Patil *et al.*, "Intriguing field-effect-transistor performance of two-dimensional layered and crystalline CrI_3," *Mater. Today Phys.*, vol. 12, pp. 100174–100199, 2020, doi: 10.1016/j.mtphys.2019.100174.

[30] K. Momma and F. Izumi, "VESTA 3 for three-dimensional visualization of crystal, volumetric and morphology data," *J. Appl. Crystallogr.*, vol. 44, pp. 1272–1276, 2011, doi: 10.1107/S0021889811038970.

[31] J. P. Perdew *et al.*, "Atoms, molecules, solids, and surfaces: Applications of the generalized gradient approximation for exchange and correlation," *Phys. Rev. B*, vol. 48, no. 7, p. 4978, 1992, doi: 10.1103/PhysRevB.48.4978.2.

[32] H. J. Monkhorst and J. D. Pack, "Special points for Brillouin-zone integrations*," *Phys. Rev. A*, vol. 13, no. 12, pp. 5188–5192, 1976, doi: https://doi.org/10.1103/PhysRevB.13.5188.

[33] G. Guo, G. Bi, C. Cai, and H. Wu, "Effects of external magnetic field and out-of-plane strain on magneto-optical Kerr spectra in CrI_3 monolayer," *J. Phys. Condens. Matter*, pp. 1–13, 2018, doi: doi.org/10.1088/1361-648X/aac96e.

[34] S. Ghosh and N. Binggeli, "Structural and magnetic response of CrI_3 monolayer to electric field," *Phys. B Condens. Matter*, vol. 570, no. May, pp. 166–171, 2019, doi: 10.1016/j.physb.2019.06.040.

[35] Q. Xu, W. Xie, Z. Lu, and Y. Zhao, "Theoretical study of enhanced ferromagnetism and tunable magnetic anisotropy of monolayer CrI_3 by surface adsorption," *Phys. Lett. A*, vol. 384, no. 29, pp. 126754–126760, 2020, doi: 10.1016/j.physleta.2020.126754.

[36] P. Bruno, "Tight-binding approach to the orbital magnetic moment and magnetocrystalline anisotropy of transition-metal monolayers," *Phys. Rev. B*, vol. 39, no. 1, pp. 865–868, 1989, doi: 10.1103/PhysRevB.39.865.

[37] V. Kumar Gudelli and G. Y. Guo, "Magnetism and magneto-optical effects in bulk and few-layer CrI_3: a theoretical GGA + U study," *New J. Phys.*, vol. 21, no. 5, 2019, doi: 10.1088/1367-2630/ab1ae9.

[38] W. Zhang, Q. Qu, P. Zhu, and C. Lam, "Robust intrinsic ferromagnetism and half semiconductivity in stable two-dimensional single-layer chromium trihalides," *J. Mater. Chem. C*, vol. 3, pp. 12457–12468, 2015, doi: 10.1039/C5TC02840J.

[39] L. Webster and J. Yan, "Strain-tunable magnetic anisotropy in monolayer $CrCl_3$, $CrBr_3$,

and CrI_3," *Phys. Rev. B*, vol. 98, no. 14, p. 144411, 2018, doi: 10.1103/PhysRevB.98.144411.

[40] I. M. Miron *et al.*, "Current-driven spin torque induced by the Rashba effect in a ferromagnetic metal layer," *Nat. Mater.*, vol. 9, no. 3, pp. 230–234, 2010, doi: 10.1038/nmat2613.

[41] J. Kim *et al.*, "Layer thickness dependences of the current-induced effective field vector in Ta | CoFeB | MgO," *Nat. Mater.*, vol. 12, no. 2, pp. 1–6, 2012, doi: 10.1038/nmat3522.

[42] E. Lesne *et al.*, "Highly efficient and tunable spin-to-charge conversion through Rashba coupling at oxide interfaces," *Nat. Mater.*, vol. 1, no. August, pp. 4–10, 2016, doi: 10.1038/NMAT4726.